5-28-2013

Dynamic Dual-Tracer MRI-Guided Fluorescence Tomography to Quantify Receptor Density In Vivo

Scott C. Davis
Dartmouth College

Kimberley S. Samkoe
Dartmouth College

Kenneth M. Tichauer
Dartmouth College

Kristian J. Sexton
Dartmouth College

Jason R. Gunn
Dartmouth College

See next page for additional authors

Dynamic dual-tracer MRI-guided fluorescence tomography to quantify receptor density in vivo

Scott C. Davis[a,1], Kimberley S. Samkoe[b], Kenneth M. Tichauer[a,c], Kristian J. Sexton[a], Jason R. Gunn[a], Sophie J. Deharvengt[d], Tayyaba Hasan[e], and Brian W. Pogue[a,b,e]

[a]Thayer School of Engineering, Dartmouth College, Hanover, NH 03755; Departments of [b]Surgery and [d]Pathology, Geisel School of Medicine at Dartmouth, Hanover, NH 03755; [c]Department of Biomedical Engineering, Illinois Institute of Technology, Chicago, IL 60616; and [e]Wellman Center for Photomedicine, Harvard Medical School, Massachusetts General Hospital, Boston, MA 02114

Edited by Rakesh K. Jain, Harvard Medical School and Massachusetts General Hospital, Boston, MA, and approved April 15, 2013 (received for review August 27, 2012)

The up-regulation of cell surface receptors has become a central focus in personalized cancer treatment; however, because of the complex nature of contrast agent pharmacokinetics in tumor tissue, methods to quantify receptor binding in vivo remain elusive. Here, we present a dual-tracer optical technique for noninvasive estimation of specific receptor binding in cancer. A multispectral MRI-coupled fluorescence molecular tomography system was used to image the uptake kinetics of two fluorescent tracers injected simultaneously, one tracer targeted to the receptor of interest and the other tracer a nontargeted reference. These dynamic tracer data were then fit to a dual-tracer compartmental model to estimate the density of receptors available for binding in the tissue. Applying this approach to mice with deep-seated gliomas that overexpress the EGF receptor produced an estimate of available receptor density of 2.3 ± 0.5 nM (n = 5), consistent with values estimated in comparative invasive imaging and ex vivo studies.

molecular imaging | oncology | optical imaging | engineered proteins | spectroscopy

Cancer pathogenesis often results in abnormal expression of cell surface receptors on the diseased cells. This pathological irregularity gives rise to a natural tumor-to-normal tissue contrast mechanism that can be exploited to disproportionately deliver toxic compounds to cancer cells. Additionally, because many of these receptors are involved in cell signaling pathways that lead to enhanced cell proliferation, reduced apoptosis, and drug resistance, they are increasingly being targeted with receptor-specific therapies that interfere with these pathways to block signaling and inhibit tumor growth. As efforts to personalize cancer treatment by targeting patients' specific receptor expression profiles expand (1–4), the ability to noninvasively quantify the availability of those receptors in living tissue would be an important development with broad implications for drug development programs and for monitoring a patient's response to therapies.

Examining receptor expression currently requires analyzing select tissue specimens extracted by biopsy or tumor tissue resection. Some of these techniques, such as immunohistochemical staining, can be used to estimate the total density of receptors in a given cancer cell population; however, an important distinction must be made between the total density of receptors in the cell population and the density of receptors available for binding in living tissue. The latter depends on the pharmacokinetics of the injected agent, the vascular and ECM structures in the tumor, the arrangement of the cancer cells, and the biochemical environment. Thus, ex vivo measurements should be thought of as a maximum potential receptor density, and likely overestimate the receptors available for targeting by therapeutic agents (5). Analyzing receptor status using tissue specimens is also subject to intratumoral heterogeneity (6) and precludes tracking of receptor density longitudinally, because repeated harvesting of tissue samples is usually infeasible. Noninvasive techniques, however, would enable monitoring of changes in cellular receptor availability in response to therapy over time, a capability applicable in both preclinical animal research and clinical practice.

Examples of receptor-targeted imaging of cancer in vivo are numerous (7–11), although few address the capacity to quantify binding kinetics and receptor availability. The bulk of these efforts involves imaging a single contrast agent, termed a tracer here, targeted to a specific receptor. Although single-tracer modalities can often produce images with enhanced tumor-to-normal tissue contrast, the measurement of tracer–receptor binding is confounded by the behavior of the tracer in the body—namely, the rates at which the tracer transports between the vascular and extravascular spaces and the rates at which it binds and becomes dissociated from the receptor—among other factors (12–15). To isolate receptor–tracer binding quantities, the works by Lammertsma and Hume (16) and Logan et al. (17) introduced compartmental modeling approaches for dynamic PET imaging of receptor kinetics in the brain. These strategies require referencing the tracer kinetics in the tissue of interest to the kinetics in a reference tissue region that has similar hemodynamics but is devoid of the targeted receptor. The required identification of a reference tissue region largely precludes the application of this approach in cancer imaging, because solid tumors have unique vasculature (12, 18–20) that alters tracer kinetics. A recent study established a more robust method applicable in any tissue region, including solid tumors, by adapting the compartmental model principle to a dual-tracer model developed around dynamic imaging of two tracers in the same tissue simultaneously (21). Although optical imaging methods are well-suited for this multitracer approach because of their ability to discriminate multiple compounds based on their spectral signatures, imaging deep-seated tumors is severely limited by photon scattering in tissue. Thus, previous experiments validating the dual-tracer modeling approach were completed using invasive, surface-weighted imaging techniques.

In this study, we report on noninvasive quantification of binding kinetics and available receptor density in deep tissue using dual-tracer MRI-coupled fluorescence molecular tomography (MRI-FMT). Previous studies have used multimodal FMT to report single-agent fluorophore kinetics in the blood pool (22) and tumor xenografts (23). The present study applies this technique to examine the quantification of specific receptor binding in vivo. Estimating this parameter is achieved by imaging the dynamics of two injected fluorescent tracers simultaneously, one tracer targeted to a specific receptor and the other a nontargeted counterpart, and

Author contributions: S.C.D., K.S.S., and B.W.P. designed research; S.C.D., K.S.S., K.J.S., J.R.G., and S.J.D. performed research; S.C.D., K.M.T., T.H., and B.W.P. analyzed data; and S.C.D. wrote the paper.

The authors declare no conflict of interest.

This article is a PNAS Direct Submission.

Freely available online through the PNAS open access option.

[1]To whom correspondence should be addressed. E-mail: scott.c.davis@dartmouth.edu.

This article contains supporting information online at www.pnas.org/lookup/suppl/doi:10.1073/pnas.1213490110/-/DCSupplemental.

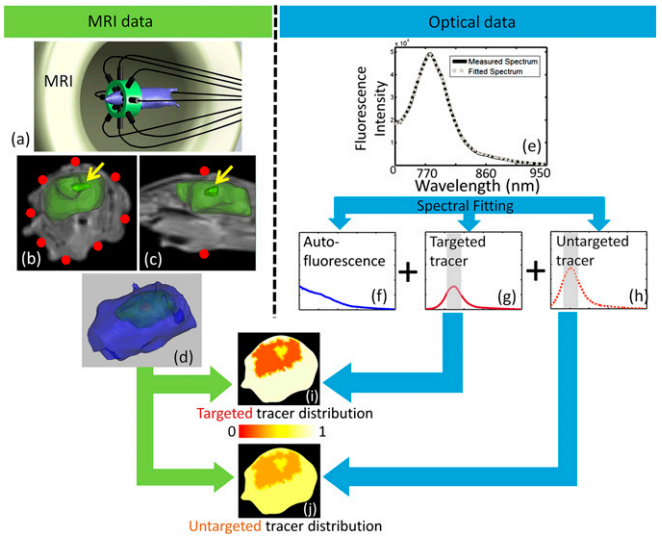

Fig. 1. Dual-tracer MRI-FMT for a single frame in a dynamic series. (*A*) Representation of the MRI-FMT animal interface inside the MRI bore. The head of the rodent (blue) is surrounded by eight optical fibers in the coronal plane. (*B*) Coronal and (*C*) sagittal slices of the MR images showing the segmented brain and tumor tissues in green. A yellow arrow points to the tumor tissue and the red dots correspond to the optical fiber positions. (*D*) Surface renderings of the mouse head (blue), brain (green), and tumor (red) used to create a finite element mesh that serves as a template for the optical image reconstructions. (*E*) A measured spectrum from a single source–detector projection is shown as a black solid line. A spectral fitting algorithm determines the relative contribution from the (*F*) tissue autofluorescence and fluorescence from the (*G*) targeted and (*H*) untargeted tracers that compose the measured spectrum. The fitted spectrum is shown as a gray dotted line in *E*. After spectral fitting of the spectra from each projection, the MRI-based finite element mesh is combined with the separated tracer data to produce volumetric images of fluorescence yield. A single slice from this volume is shown in *I* and *J* for the targeted and untargeted tracers, respectively.

fitting the time-dependent tracer concentrations to a dual-tracer compartmental model describing the pharmacokinetics of the tracers (*Materials and Methods*). Of particular interest is the binding potential (*BP*), a parameter defined as the product of the concentration of receptors available for binding, B_{avail}, and the affinity of the targeted tracer to the receptor, k_a:

$$BP = k_a B_{avail}. \quad [1]$$

Thus, *BP* is a unitless quantity proportional to the receptor–target affinity (in Molar^{-1}) and density of receptors available to bind with the targeted tracer (in Molar). Because k_a can often be determined a priori using in vitro techniques, the capacity to dynamically image targeted and nontargeted tracers simultaneously facilitates the recovery of B_{avail} in living tissue.

Results

A key requirement for deploying the dual-tracer strategy is the ability to image the dynamics of two tracers in tissue. The MRI-FMT system presented here is capable of distinguishing multiple fluorophores measured simultaneously by using spectrally resolved optical detection. This dual-tracer imaging approach is realized by acquiring multiple projections of data through the tissue volume, each of which is a highly resolved spectrum composed of fluorescence signals from the different fluorescent compounds in the tissue, illustrated in Fig. 1*E*. Provided that the fluorophores have distinct emission spectra, a spectral fitting algorithm applied to each spectrum extracts the contribution of each fluorescent compound to the measured spectrum, effectively separating signals emitted from the tissue autofluorescence and any number of fluorescent tracers in the tissue (Fig. 1 *F–H*). The fluorescent dyes used in this study were IRDye 800CW (LI-COR Biosciences) and Alexa Fluor 750 (Life Technologies), with emission peak maxima at ~800 and 775 nm, respectively. After the signals are separated, the internal distribution of each tracer can be estimated by fitting the projection data to a numerical model based on the diffusion approximation of light propagation in tissue (24–28). Applying these principles, imaging fluorescence activity in relatively large tissue volumes (over 5 cm) is feasible. Substantial evidence exists suggesting that volumetric images of fluorescence activity are more accurate if additional information, such as the anatomical features of the tissue, is incorporated in the optical image reconstruction algorithm (29–34). To that end, the hybrid MRI-FMT system used in this study integrates the optical detection channels into a specialized MRI insert, an arrangement that facilitates the merging of the optical projection data and MR image stacks. An illustration of this process is shown in Fig. 1 and described in *Materials and Methods*.

To show the ability to separate and image two colocalized tracers in a realistic volume, a cylindrical tissue-simulating phantom was imaged with the MRI-FMT system. The 27-mm-diameter phantom was constructed of epoxy resin containing titanium dioxide and India ink to mimic the optical scattering and absorption properties typically found in living tissue. To simulate a tumor region, a 6-mm-diameter hole drilled axially between the edge and the center of the cylinder was filled with 1% (vol/vol) intralipid, which mimics optical scatter in tissue, and different concentrations of the two imaging tracers. In this experiment, the concentration of IRDye 800CW was held constant at 100 nM, whereas the concentration of the Alexa Fluor 750 dye was varied from 1 to 100 nM , and the phantom was imaged at each concentration. The image series for both fluorescent dyes are presented in Fig. 2*A*, and show that there was very little variation in fluorescence activity in the IRDye800CW channel, whereas the activity in the Alexa Fluor 750 channel had a clear dependence on changes in concentration. A plot of the recovered values in the region of interest as a function of Alexa Fluor 750 concentration is shown Fig. 2*B*, and confirms a significant linear response in the Alexa Fluor 750 channel, $R^2 = 0.99$, whereas the IRDye800 channel remained relatively flat

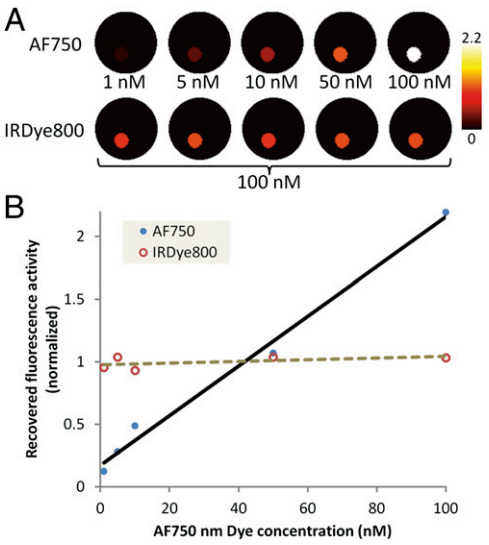

Fig. 2. Dual-tracer MRI-FMT imaging of a tissue-mimicking phantom. (*A*) Recovered images of fluorescence yield (normalized to the mean of the IRDye800 channel) from colocalized Alexa Fluor 750 and IRDye800CW. (*B*) Normalized values of fluorescence yield in the region of interest plotted as a function of Alexa Fluor 750 concentration. The IRDye800CW concentration was held constant at 100 nM for each concentration of Alexa Fluor 750.

(SD = 5%). Because of the differences in the excitation absorbance and the quantum yield between the two dyes, the dominant signal in the measured spectra transitioned between IRDye 800CW fluorescence and Alexa Fluor 750 fluorescence as the Alexa Fluor concentrations were increased, showing the ability of the spectral fitting technique to accurately extract weak signals of either dye from dominant background signals. Finally, we showed that interchannel cross-talk is between 0% and 4% by examining the spectral fitting results from phantoms containing a single tracer, which is described in *SI Text*.

To investigate the capacity of dynamic dual-tracer MRI-FMT to quantify the density of available receptors in a deep-seated tumor model, athymic nude mice with U251 brain tumors were imaged using the dynamic imaging protocol (*SI Text* has cell line and animal preparation details). U251 tumor cells have been reported to have elevated expression of EGF receptor (EGFR) (35). This receptor is associated with a number of cellular processes that maintain cancer cell proliferation, is commonly overexpressed in clinical cancers (36–39), and thus is a natural drug target (38, 40). Anesthetized mice positioned in the MRI-FMT system were scanned pre- and postgadolinium (Gd) contrast with a T1-weighted MRI sequence and then administered a solution containing 0.2 nmol of each optical tracer (targeted and untargeted) in the tail vein. The targeted tracer used in this experiment was Affibody anti-EGFR imaging agent (Affibody) conjugated to Licor IRDye 800CW fluorescent dye. This anti-EGFR imaging agent is a three-helix protein engineered to bind to EGFR with low nanomolar affinity (41). The untargeted counterpart was Affibody negative control, which maintains the same three-helix structure and size as the anti-EGFR agent and shows no binding affinity to EGFR. This negative control agent was conjugated to the AlexaFluor 750 fluorescent dye (*SI Text* has details on tracer selection and preparation). Dynamic FMT imaging began immediately after injection and continued over the course of 1 h at a rate of approximately one frame per 2 min for a total of 27 frames. For each frame of data, the signals from each dye were separated into two optical data channels using the spectral fitting technique. Applying the anatomical structure from the MR image stack in the optical image reconstruction algorithm provided volumetric images of fluorescence activity for each tracer at each frame, resulting in a time series of 27 images for each tracer. This process is illustrated by the diagram in Fig. 3 and detailed further in *Materials and Methods*.

A sampling of the time series images recovered for one animal is presented in Fig. 4. For display purposes, each frame in the image series is presented as a 2D coronal slice interpolated from the 3D volume. The position of this slice with respect to the tissue volume is illustrated in Fig. 4*A*, and the corresponding MR image is presented in Fig. 4*B*. The tumor region, as defined by contrast-enhanced MRI, is outlined in green in Fig. 4*B*. A sample of the FMT image time series for both targeted and untargeted fluorescent tracers is shown in Fig. 4 *C* and *D*, respectively. Because the images were acquired shortly after injection, the tracer concentrations were relatively high throughout the tissue. Although the normal tissues outside the brain show the highest fluorescence uptake levels, the tumor region in the brain shows obvious enhancement compared with the normal brain tissue. There was relatively little fluorescence activity in the brain tissue itself. These observations were consistent between all five animals.

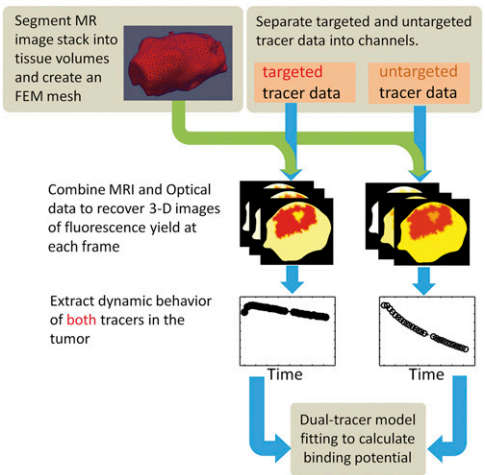

Fig. 3. Procedure for recovering binding potential using dynamic dual-tracer MRI-FMT.

To determine the binding potential of the anti-EGFR Affibody tracer, the kinetics of both tracers in the tumor region were extracted from the image sequences. The coronal MRI slices shown in Fig. 4*E* illustrate the anatomical structure near the imaging plane in each mouse. The overlaid outlines in Fig. 4*E* identify the tumor region defined by Gd contrast enhancement. Normalized dual-tracer time series data for the tumor region in all animals are presented in Fig. 4*F*. These data are consistent between all animals and show very different pharmacokinetic behavior between the anti-EGFR and negative control tracers. The Affibody negative control tracer experienced rapid uptake immediately after injection that was not captured by the image sequence at the acquisition rate used. This uptake was followed by a steady clearance that reduced the drug concentration by 52% (mean for all animals, ±8% SD) by the end of the 1-h imaging session. In contrast, the targeted anti-EGFR Affibody tracer showed less rapid uptake and much slower clearance that reduced the fluorescence activity in the tumor by less than 13% (mean for all animals, ±4% SD) from maximum over the course of 1 h. The time series data were used to fit the parameters of the dual-tracer compartment model to determine values of binding potential in the tumor. The result was a mean binding potential of 0.80 ± 0.17 in the population of mice (n = 5). Applying Eq. **1** reveals an available receptor density of 2.3 ± 0.5 nM for $k_a = 0.36 \times 10^9$ M^{-1} for the Affibody probe.

To validate the binding potential values calculated using the MRI-FMT image series, exposed s.c. U251 tumors were imaged using a planar fluorescence scanner in a separate population of mice. Selected images from the dynamic imaging session for one animal are shown in Fig. 5, with the targeted and untargeted tracer image series in Fig. 5 *A* and *B*, respectively. The average fluorescence values in the tumor region, delineated manually, were calculated to produce the time curves shown in Fig. 5*C*. Binding potential values were calculated in the same manner as the *BP* values from the MRI-FMT imaging data, resulting in a mean value of 0.90 ± 0.23 and thus, an available receptor density of 2.5 ± 0.6 nM for all animals (n = 5).

Because receptor expression can be influenced by the site of tumor growth, immunoblotting was used to compare EGFR expression between s.c. and intracranial U251 tumors (*SI Text*). Although these data show very similar expressions between growth sites [0.29 ± 0.12 and 0.23 ± 0.1 for s.c. (n = 6) and intracranial (n = 4) tumors, respectively], total receptor expression is only loosely related to the availability of receptors in vivo. Therefore, to further validate the MRI-FMT results in intracranial tumors, a single-time point method to approximate binding potential was applied to ex vivo slices of intracranial U251 tumors. This approximation, detailed in *Materials and Methods*, results in a simple relationship between binding potential and the ratio of the targeted to untargeted dye fluorescence. Available receptor density values recovered using this method were 2.3 ± 1.5 (n = 6).

Discussion

The binding potential values recovered using MRI-FMT are in close agreement with those values determined using planar imaging,

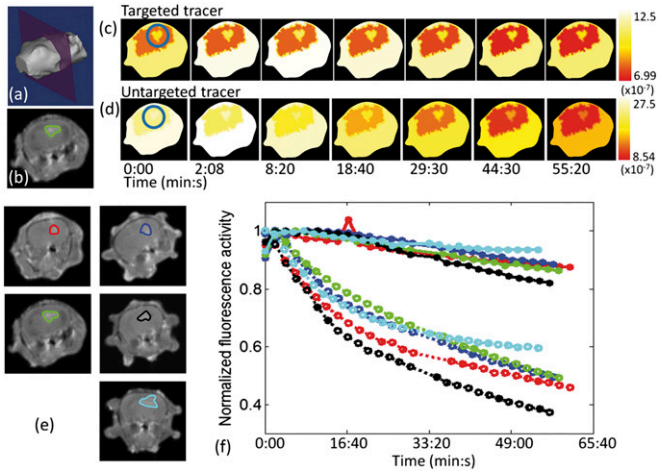

Fig. 4. Dynamic dual-tracer MRI-FMT imaging of gliomas in mice. (*A*) 3D rendering of a study mouse with an intersecting plane illustrating the location of the coronal image slices in *B*–*D*. (*B*) A coronal MRI image of the mouse head with the tumor region outlined in green. This image slice corresponds to the time series images showing fluorescence activity of the (*C*) targeted and (*D*) untargeted tracers. (*E*) Coronal MRI images of all five study animals with overlay outlines of the tumor region. (*F*) Time series of fluorescence activity of targeted (● solid lines) and untargeted (○ dotted lines) tracers in the tumors of all animals. The targeted and nontargeted curves for each animal are paired by color, which also corresponds to the colors of the outlined tumor regions in *E*.

suggesting that accurate noninvasive imaging of binding potential in vivo is feasible. These results were further validated by using the recovered binding potential values to compute the density of available receptors and comparing them with previously reported values. Tichauer et al. (21) previously reported in vivo binding potential values between EGFR and EGF for s.c. U251 tumors. EGF is the natural ligand to EGFR and has a higher affinity for the receptor than the anti-EGFR Affibody molecule used herein. Applying Eq. **1** to compensate for different affinities results in similar values for available receptor density: $B_{avail} = 2.0 \pm 0.4$, 2.3 ± 0.5, 2.3 ± 1.5, and 2.5 ± 0.6 nM for measurements acquired by Tichauer at al. (21), MRI-FMT, ex vivo analysis of intracranial tumors, and planar imaging reported herein, respectively.

The close proximity of B_{avail} values measured with different imaging paradigms, with different targeted tracers, and in tumors implanted in different tissue types exemplifies the robustness of the dual-tracer approach. Subcutaneous tumors often have very different vasculature than tumor models grown directly in their native organ (in this case, the brain). Growth site-specific vasculature may explain the differences in the observed pharmacokinetic behavior of the tracers in organ-implanted and s.c. tumors (Figs. 4*F* and 5*C*, respectively). Despite these observed differences, both tracers inhabit the same vascular and extravascular space, and the density of available receptors was found to be consistent, regardless of tumor implantation site. Single-tracer approaches under these conditions are unable to adequately compensate for differences in vascularity, making reliable recovery of available receptor density nearly intractable.

Our findings suggest that dual-tracer quantification of binding potential is a robust technique that mitigates many of the complex calibration procedures required for quantitative single-tracer imaging. Because the model operates on the normalized ratios of two tracers injected simultaneously, quantifying *BP* is independent of many of the parameters that challenge imaging a single tracer, a process that often requires absolute instrument calibration. Thus, the approach is unaffected by commonly confounding factors, such as variation in tissue optical properties, optical coupling into and out of the tissue, concentration of tracer administered, and fluorophore quantum yield. Insensitivity to these parameters is a clear advantage for imaging approaches founded on measurement ratios. Practically, the only requirements are that the optical properties at the emission wavelengths of both tracers are similar and that the two tracers have similar pharmacokinetic behavior in vivo, excluding binding. The former is certainly the case given the proximity of the fluorescence emission wavelengths of the tracers. The latter requires careful choice of the tracer compounds, with consideration given to factors such as molecular weight, conjugate binding chemistry, and potential for nonspecific binding.

The observed robustness of the dual-tracer modeling approach is valid provided that a number of assumptions are met. As discussed elsewhere (21), the model system assumes first-order binding kinetics and therefore loses accuracy when a large percentage of receptors are bound with targeted tracer. Although receptor saturation may obtain if large quantities of tracer are administered, an analysis of plasma and binding kinetics, and receptor density in the U251 tumor line shows that receptor saturation at the injected dose used herein (0.2 nmol) is unlikely (*SI Text*). In addition to first-order kinetics, the model assumes that the concentrations of bound and unbound targeted tracer in the extravascular space are in instantaneous equilibrium. Although fundamental to the derivation of this model system, values of binding potential have been shown to be robust even when this assumption does not apply (42, 43). Additional physiological processes, such as tracer metabolism and receptor internalization, are not captured by the model and therefore represent potential sources of error in the calculations of *BP*. However, because the model operates on data acquired within a short time frame after injection, the impact of these factors is likely minimal, an assertion supported by previous work (5). Finally, although most system-specific biases are mitigated, the significant depth-dependent sensitivity of FMT remains a limitation for imaging smaller structures and pathologies deep within tissue, even when guided by complementary imaging modalities, and could introduce cross-talk between tissue regions. As a result, visualizing submillimeter spatial variations in binding potential within a deep-seated tumor will likely be infeasible. Despite this limitation, quantifying the average available receptor density in tumor masses is achievable in research animals, and the recent history of FMT studies in the human breast (24, 44) suggests that translating the technology to clinical imaging is feasible for tissue organs accessible by FMT imaging geometries.

The noninvasive quantification of binding potential, and thus density of available cell surface receptors, shown here represents an important advancement towards patient-specific cancer treatment. Costly preclinical drug development studies would benefit from longitudinal monitoring of receptor binding in response to candidate compounds, and the ability to stratify patients enrolling in

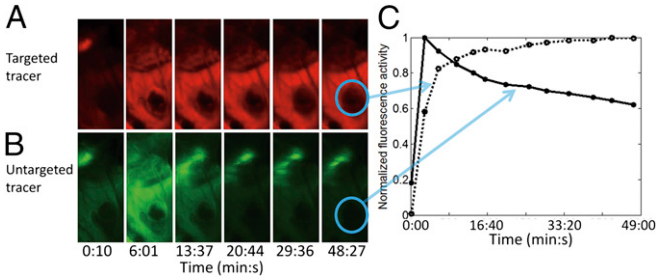

Fig. 5. Dynamic dual-tracer planar imaging of an s.c. tumor. Planar fluorescence images of exposed U251 tumor and surrounding normal tissue in a living mouse for (*A*) targeted and (*B*) untargeted tracers. (*C*) Time series data for the average fluorescence activity in the tumor region for targeted (dotted line and open circles) and untargeted (solid line and solid circles) tracers.

clinical trials based on their receptor expression profiles would help economize those programs. Additionally, monitoring patient response to approved target-specific drugs would enable the tailoring of treatment regimens and provide actionable information on drug resistance. Although our work has focused on cancer pathologies, the platform is broadly applicable to other disease states that involve overexpression of cellular receptors or specific binding in general, such as Alzheimer's disease or infection, and thus may play a significant role in the growing efforts towards personalized care.

Materials and Methods

Dual-Tracer Binding Potential Model. Derivation of the dual-tracer model system has been described elsewhere (21). Briefly, the behavior of the targeted tracer in this model is defined by a series of rate constants that describe the movement of the tracer between the blood plasma and extravascular space and once the tracer is in the extravascular space, the rates at which it will bind to and be released from the available receptors. Because the nontargeted tracer is assumed to have no binding affinity, its behavior is defined by rate constants that describe the tracer movement between the blood plasma and extravascular spaces only. If the two tracers have similar rates of extravasation, the differential equations that describe the behavior of both tracers can be combined and reduced to a single expression that depends only on the concentrations of both tracers (measureable), the ratio of the extravasation rates of both tracers, the intravasation rate of the targeted tracer, and the binding potential (*BP*) of the tracer–receptor pair:

$$F_T(r,t) = R_1 F_{UT}(r,t) + \left(k_2 - \frac{R_1 k_2}{1+BP}\right) F_{UT}(r,t) * e^{-\frac{k_2 t}{1+BP}},$$

where the fluorescence activity of the targeted and untargeted tracers is given by F_T and F_{UT}, respectively, R_1 is the ratio of rate constants that describes the transport of the targeted and untargeted tracers from the vasculature to the extravascular space, and k_2 is the rate constant for targeted tracer to transport from the extravascular space back into the vasculature. F_T and F_{UT} can be measured by dynamic imaging of both tracers, and the remaining parameters fitted using a nonlinear least-squares algorithm applied to the expression above.

Dynamic MRI-FMT Experimental Procedure. The hybrid MRI-coupled FMT system has been described extensively in previous publications (29, 30, 45, 46).

Each animal was imaged with Gd-MRI at least 2 d before the MRI-FMT scans. Only animals with visible Gd-enhanced features in the brain were included in the study. The MRI-FMT imaging procedure began by positioning an anesthetized (1.5% isoflurane, 1 L/min oxygen) mouse in the MRI-FMT rodent coil and placing the optical fibers in contact with the head. A series of MRI scout scans were used to confirm that the plane of the optical fibers intersected the tumor volume; in some cases, animal repositioning was required. After a satisfactory position was established, a full set of pre- and post-Gd contrast T1-weighted images was acquired over the volume of the head. Under static FMT imaging conditions, the FMT imaging would be completed during the MR acquisition; however, to simplify the process, dynamic FMT images were started after the MR scans were completed without changing the animal position.

Dynamic FMT imaging began immediately after tail vein administration of a solution containing both fluorescent tracers (0.2 nmol of each). These measurements were acquired continuously over the course of 1 h after administration at a rate of approximately 1 frame per 2 min for a total of 27 frames. Each frame of data consisted of 56 source–detector pairs (8 sources and 7 detectors). Under normal static FMT imaging conditions, a set of excitation measurements corresponding to the fluorescence emission measurements is acquired to calibrate the data to the model and normalize internal heterogeneities in optical properties. To reduce the per-frame acquisition time, only two excitation measurements were collected for each animal: one before tracer administration and the other between frames 15 and 16 during the dynamic fluorescence emission measurements.

MRI-FMT Data Processing and Image Recovery. The dual-tracer MRI-FMT image recovery procedure involves processing and merging MRI and optical data. A diagram of this procedure for one imaging frame in a dynamic sequence is presented in Fig. 1. For reference, Fig. 1*A* shows a rendering of an animal subject [rendered from the Mouse Whole Body (MOBY) phantom (47) and shown in blue] in the MRI–optical interface. Eight optical fibers surrounding the head transmit light to and from the tissue. Image processing began by segmenting the T1-weighted Gd-enhanced MRI images into three regions using MIMICS software (Materialise Medical Software): the tumor region as defined by Gd enhancement, a normal brain region, and the rest of the tissue volume. Fig. 1 *B* and *C* show coronal and sagittal MRI slices of one of the study animals with volumetric renderings of the brain and tumor regions. Also shown are the fiber positions (Fig. 1 *B*, red dots and *C*, red dots). From these volumetric segmented regions, shown together in Fig. 1*D*, a 3D finite element mesh (~15,000 nodes) compatible with the optical image recovery algorithms was created.

Data for an optical imaging frame in the dynamic MRI-FMT sequence consist of 56 fluorescence emission spectra similar to the one shown in Fig. 1*E*, solid black curve. Each measured spectrum is composed of the overlapping emission spectra from the two fluorophores and the tissue autofluorescence. To image the internal distribution of each tracer independently, the emission signals from each must be extracted from the measured spectrum. This spectral discrimination was accomplished using a linear least-squares spectral fitting algorithm, which uses premeasured basis spectra to extract individual fluorescent sources, a procedure described in previous publications (29, 45, 48–50) and illustrated in Fig. 1 *E*–*H*. The basis spectra used here include the tissue autofluorescence spectra measured from mice before dye administration (Fig. 1*F*) and the fluorescence emission peaks of the two tracers measured independently in tissue phantoms (Fig. 1 *G* and *H*). The fitted spectrum shown in Fig. 1*E*, gray dotted curve, represents the sum of the spectral components in Fig. 1 *F*–*H* extracted using the spectral fitting routine. After the contribution of each tracer's emission spectra was extracted from the measured spectrum, the peaks were integrated to provide a single intensity value for each tracer. This analysis was repeated for each source–detector pair, producing 56 optical data points for each tracer and a single frame.

The optical and MRI data flows merge in the image recovery algorithm as described extensively elsewhere (30, 45, 51). Briefly, this process involves fitting the optical data measured on the tissue boundary to a numerical model based on the diffusion approximation of photon propagation in tissue. The finite element mesh created from the MRI image stack serves as the numerical template on which the optical images are recovered. Before image reconstruction, the fluorescence data were calibrated to the model using the excitation measurements acquired during the imaging sequence, a process described elsewhere (45). Images were recovered using the hard-priors approach, which operates under the assumption that the fluorescence activity is homogeneously distributed in a given internal tissue region. This approach dramatically reduces the number of unknowns in the image recovery process.

The culmination of this procedure is two volumetric images of fluorescence activity: one for each tracer per frame. Two dimensional slices from the 3D volumes are shown in Fig. 1 *I* and *J* for the targeted and untargeted tracers, respectively. Image reconstructions for both tracers were repeated for each frame in the dynamic series, although because the animal did not move during the length of the MRI and optical scans, a single MRI-derived Finite Element Method (FEM) mesh was used for all frames from an animal subject. In total, the fully processed imaging results for each animal consisted of 27 frames of 3D fluorescence yield images for both fluorescent tracers—a total of 54 images per animal. The values reported in these images were used in the reference tracer model to extract values of binding potential.

Planar Imaging Experiments. Imaging was performed by scanning exposed tumors with a dual-channel Licor Odyssey fluorescence scanner (Licor). The animal subjects were anesthetized by i.p. administration of 100:10 mg/kg ketamine:xylazine, and an incision was made in the skin to expose the tumor mass and surrounding tissue. The animals were then positioned on a glass slide on the imaging surface of the fluorescence scanner, with the exposed tissue contacting the glass. Because of the hardware configuration of the Odyssey instrument, which acquires dual-channel fluorescence images at 700 and 800 nm, the Affibody negative control imaging agent was conjugated to Licor IRDye 680RD rather than Alexa Fluor 750, which was used in the MRI-FMT experiments. After the animal was positioned and an initial baseline scan was acquired, a 100 μL solution containing 0.1 nmol of each tracer was injected into the tail vein, and imaging scans started immediately. Each dual-channel scan of the animal was completed in 40 s, and these scans were acquired every 3–5 min over the course of 50 min. A total of 13 dual-channel frames was acquired for each animal.

After acquisition, the images were processed to produce average binding potential values in the tumors of each animal. For each animal, a tumor region was identified by manual inspection in the fluorescence image sequences of both tracers. Average values of fluorescence intensity in the tumor region were then extracted from each frame, producing a time series of fluorescence intensity in the tumor for both fluorescence tracers. The time

course data from both channels were then fit to the parameters of the reference tracer model to determine binding potential.

Ex Vivo Quantification of Available Receptor Density in Orthotopic Tumors. An ex vivo method to approximate binding potential (21) was applied to intracranial tumors. This approximation is enabled by two additional assumptions, namely that the contribution from the plasma is negligible (which is generally the case several minutes after injection given the low volume of plasma in the tissue) and that the two tracers behave identically in the tissue, with the exception of binding. Provided that these assumptions apply, it can be shown that the dual-tracer model reduces to

$$BP = F_T / F_{UT} - 1, \quad [2]$$

enabling *BP* to be estimated with a simple ratio of the targeted and untargeted tracers from a single dual-channel image. Relaxing the requirement to acquire dynamic measurements of tracer kinetics in the tumor allows the analysis to be completed with ex vivo specimens, and thus, it provides an independent method to validate *BP* values in tumors inaccessible to in vivo planar imaging. This approach was applied to ex vivo slices of intracranial U251 tumors and compared with the MRI-FMT imaging results. Details on the experimental procedure and data processing used for this study can be found in *SI Text, Ex Vivo Quantification of Available Receptor Density in Orthotopic Tumors*.

ACKNOWLEDGMENTS. This work was funded by National Institutes of Health Grants R01CA109558 (to S.C.D. and B.W.P.), R01CA156177 (K.S.S., J.R.G., T.H., and B.W.P.), and U54CA151662 (to K.M.T., K.J.S., and B.W.P.) as well as Department of Defense Award W81XWH-09-1-0661 (to S.C.D.).

1. Deschoolmeester V, Baay M, Specenier P, Lardon F, Vermorken JB (2010) A review of the most promising biomarkers in colorectal cancer: One step closer to targeted therapy. *Oncologist* 15(7):699–731.
2. Rosen MJ, Heniford BT (2005) Endoluminal gastric surgery: The modern era of minimally invasive surgery. *Surg Clin North Am* 85(5):989–1007.
3. Sharma SV, Settleman J (2010) Exploiting the balance between life and death: Targeted cancer therapy and "oncogenic shock." *Biochem Pharmacol* 80(5):666–673.
4. van't Veer LJ, Bernards R (2008) Enabling personalized cancer medicine through analysis of gene-expression patterns. *Nature* 452(7187):564–570.
5. Samkoe Ks, et al. (2012) High vascular delivery of EGF, but low receptor binding rate is observed in AsPC-1 tumors as compared to normal pancreas. *Mol Imaging Biol* 14: 472–479.
6. Gerlinger M, et al. (2012) Intratumor heterogeneity and branched evolution revealed by multiregion sequencing. *N Engl J Med* 366(10):883–892.
7. Gambhir SS (2002) Molecular imaging of cancer with positron emission tomography. *Nat Rev Cancer* 2(9):683–693.
8. James ML, Gambhir SS (2012) A molecular imaging primer: Modalities, imaging agents, and applications. *Physiol Rev* 92(2):897–965.
9. Massoud TF, Gambhir SS (2003) Molecular imaging in living subjects: Seeing fundamental biological processes in a new light. *Genes Dev* 17(5):545–580.
10. Weissleder R, Mahmood U (2001) Molecular imaging. *Radiology* 219(2):316–333.
11. Weissleder R, Ntziachristos V (2003) Shedding light onto live molecular targets. *Nat Med* 9(1):123–128.
12. Jain RK (2001) Delivery of molecular and cellular medicine to solid tumors. *Adv Drug Deliv Rev* 46(1-3):149–168.
13. Orcutt KD, Rhoden JJ, Ruiz-Yi B, Frangioni JV, Wittrup KD (2012) Effect of small-molecule-binding affinity on tumor uptake in vivo: A systematic study using a pretargeted bispecific antibody. *Mol Cancer Ther* 11(6):1365–1372.
14. Schmidt MM, Wittrup KD (2009) A modeling analysis of the effects of molecular size and binding affinity on tumor targeting. *Mol Cancer Ther* 8(10):2861–2871.
15. Thurber GM, Schmidt MM, Wittrup KD (2008) Factors determining antibody distribution in tumors. *Trends Pharmacol Sci* 29(2):57–61.
16. Lammertsma AA, Hume SP (1996) Simplified reference tissue model for PET receptor studies. *Neuroimage* 4(3 Pt 1):153–158.
17. Logan J, et al. (1996) Distribution volume ratios without blood sampling from graphical analysis of PET data. *J Cereb Blood Flow Metab* 16(5):834–840.
18. Jain RK (2005) Normalization of tumor vasculature: An emerging concept in antiangiogenic therapy. *Science* 307(5706):58–62.
19. Maeda H, Wu J, Sawa T, Matsumura Y, Hori K (2000) Tumor vascular permeability and the EPR effect in macromolecular therapeutics: A review. *J Control Release* 65(1–2): 271–284.
20. Minchinton AI, Tannock IF (2006) Drug penetration in solid tumours. *Nat Rev Cancer* 6(8):583–592.
21. Tichauer KM, et al. (2012) In vivo quantification of tumor receptor binding potential with dual-reporter molecular imaging. *Mol Imaging Biol* 14(5):584–592.
22. Leuschner F, et al. (2011) Therapeutic siRNA silencing in inflammatory monocytes in mice. *Nat Biotechnol* 29(11):1005–1010.
23. Lin Y, Thayer D, Nalcioglu O, Gulsen G (2011) Tumor characterization in small animals using magnetic resonance-guided dynamic contrast enhanced diffuse optical tomography. *J Biomed Opt* 16(10):106015.
24. Corlu A, et al. (2007) Three-dimensional in vivo fluorescence diffuse optical tomography of breast cancer in humans. *Opt Express* 15(11):6696–6716.
25. Milstein AB, et al. (2003) Fluorescence optical diffusion tomography. *Appl Opt* 42(16): 3081–3094.
26. Ntziachristos V, et al. (2004) Visualization of antitumor treatment by means of fluorescence molecular tomography with an annexin V-Cy5.5 conjugate. *Proc Natl Acad Sci USA* 101(33):12294–12299.
27. Ntziachristos V, Tung CH, Bremer C, Weissleder R (2002) Fluorescence molecular tomography resolves protease activity in vivo. *Nat Med* 8(7):757–760.
28. Ntziachristos V, Weissleder R (2001) Experimental three-dimensional fluorescence reconstruction of diffuse media by use of a normalized Born approximation. *Opt Lett* 26(12):893–895.
29. Davis SC, et al. (2007) Image-guided diffuse optical fluorescence tomography implemented with Laplacian-type regularization. *Opt Express* 15(7):4066–4082.
30. Davis SC, et al. (2010) Comparing implementations of magnetic-resonance-guided fluorescence molecular tomography for diagnostic classification of brain tumors. *J Biomed Opt* 15(5):051602–051610.
31. Hyde D, et al. (2009) Hybrid FMT-CT imaging of amyloid-beta plaques in a murine Alzheimer's disease model. *Neuroimage* 44(4):1304–1311.
32. Kepshire D, et al. (2009) A microcomputed tomography guided fluorescence tomography system for small animal molecular imaging. *Rev Sci Instrum* 80(4):043701.
33. Lin Y, et al. (2011) A photo-multiplier tube-based hybrid MRI and frequency domain fluorescence tomography system for small animal imaging. *Phys Med Biol* 56(15): 4731–4747.
34. McCann CM, et al. (2009) Combined magnetic resonance and fluorescence imaging of the living mouse brain reveals glioma response to chemotherapy. *Neuroimage* 45(2): 360–369.
35. Gibbs-Strauss SL, et al. (2010) Detecting epidermal growth factor receptor tumor activity in vivo during cetuximab therapy of murine gliomas. *Acad Radiol* 17(1):7–17.
36. Carpenter G (1987) Receptors for epidermal growth factor and other polypeptide mitogens. *Annu Rev Biochem* 56(1):881–914.
37. Ciardiello F, Tortora G (2001) A novel approach in the treatment of cancer: Targeting the epidermal growth factor receptor. *Clin Cancer Res* 7(10):2958–2970.
38. Marshall J (2006) Clinical implications of the mechanism of epidermal growth factor receptor inhibitors. *Cancer* 107(6):1207–1218.
39. Mendelsohn J, Baselga J (2003) Status of epidermal growth factor receptor antagonists in the biology and treatment of cancer. *J Clin Oncol* 21(14):2787–2799.
40. Ciardiello F, et al. (1996) Antitumor activity of combined blockade of epidermal growth factor receptor and protein kinase A. *J Natl Cancer Inst* 88(23):1770–1776.
41. Friedman M, et al. (2008) Directed evolution to low nanomolar affinity of a tumor-targeting epidermal growth factor receptor-binding affibody molecule. *J Mol Biol* 376(5):1388–1402.
42. Lammertsma AA, et al. (1996) Comparison of methods for analysis of clinical [11C] raclopride studies. *J Cereb Blood Flow Metab* 16(1):42–52.
43. Zhou M, et al. (1993) Real-time measurements of kinetics of EGF binding to soluble EGF receptor monomers and dimers support the dimerization model for receptor activation. *Biochemistry* 32(32):8193–8198.
44. van de Ven S, et al. (2010) A novel fluorescent imaging agent for diffuse optical tomography of the breast: First clinical experience in patients. *Mol Imaging Biol* 12(3): 343–348.
45. Davis SC, et al. (2008) Magnetic resonance-coupled fluorescence tomography scanner for molecular imaging of tissue. *Rev Sci Instrum* 79(6):064302.
46. Davis SC, et al. (2010) MRI-coupled fluorescence tomography quantifies EGFR activity in brain tumors. *Acad Radiol* 17(3):271–276.
47. Segars WP, Tsui BMW, Frey EC, Johnson GA, Berr SS (2004) Development of a 4-D digital mouse phantom for molecular imaging research. *Mol Imaging Biol* 6(3): 149–159.
48. Mansfield JR, Gossage KW, Hoyt CC, Levenson RM (2005) Autofluorescence removal, multiplexing, and automated analysis methods for in-vivo fluorescence imaging. *J Biomed Opt* 10(4):41207.
49. Xu H, Kuo C, Rice B (2008) Improved sensitivity by applying spectral unmixing prior to fluorescent tomography. *Biomedical Optics (BIOMED)* (Optical Society of America, St. Petersburg, FL).
50. Zacharakis G, Favicchio R, Simantiraki M, Ripoll J (2011) Spectroscopic detection improves multi-color quantification in fluorescence tomography. *Biomed Opt Express* 2(3):431–439.
51. Dehghani H, et al. (2008) Near infrared optical tomography using NIRFAST: Algorithm for numerical model and image reconstruction. *Commun Numer Methods Eng* 25(6): 711–732.